Geophysical Research Letters

Key Points:
- Pi2 pulsations in two frequency bands (7.6–9.2 and 12–17 mHz) detected in the magnetosheath
- These pulsations were locally generated by the Jet's After-Flow
- Similar pulsations inside the magnetosphere are directly associated with the ones in the magnetosheath

Correspondence to:

C. Katsavrias,
ckatsavrias@phys.uoa.gr

On the Generation of Pi2 Pulsations due to Plasma Flow Patterns Around Magnetosheath Jets

C. Katsavrias[1] , **S. Raptis[2]** , **I. A. Daglis[1,3]** , **T. Karlsson[2]** , **M. Georgiou[1]**, and **G. Balasis[4]**

[1]Department of Physics, National and Kapodistrian University of Athens, Athens, Greece, [2]Division of Space and Plasma Physics, School of Electrical Engineering and Computer Science, KTH Royal Institute of Technology, Stockholm, Sweden, [3]Hellenic Space Center, Athens, Greece, [4]National Observatory of Athens, Athens, Greece

Abstract We report observations of a magnetosheath jet followed by a period of decelerated background plasma. During this period, THEMIS-A magnetometer showed abrupt disturbances which, in the wavelet spectrum, appeared as prominent and irregular pulsations in two frequency bands (7.6–9.2 and 12–17 mHz) within the Pi2 range. The observations suggest—for the first time to our knowledge— that these pulsations were locally generated by the abrupt magnetic field changes driven by the jet's interaction with the ambient magnetosheath plasma. Furthermore, similar pulsations, detected by THEMIS-D inside the magnetosphere with a 140 s time-lag (which corresponds to the propagation time of a disturbance traveling with Alfvénic speed), are shown to be directly associated with the ones in the magnetosheath, which raises the question of how exactly these pulsations are propagated through the magnetopause.

Plain Language Summary The Earth's magnetosheath is particularly a turbulent region even during steady solar wind conditions. It is permeated both by waves that have been transmitted through the bow shock, as well as by fluctuations that have been generated locally. Jets in the magnetosheath can drive various wave species, especially via interaction with the magnetopause, and can have a significant magnetospheric effect. In this work, we report—for the first time—the generation of ultralow frequency waves generated, not by the jet itself but, with the jet's interaction with the ambient magnetosheath plasma. We further show that similar pulsations, which are detected inside the magnetosphere, are directly associated with the ones in the magnetosheath, which raises the question of how exactly these pulsations are propagated through the magnetopause.

1. Introduction

The Earth's magnetosheath—the region downstream of the bow shock—contains decelerated and compressed solar wind plasma exhibiting strong fluctuations in velocity, density, and associated magnetic field. Especially the magnetosheath downstream of the quasi-parallel shock, where the angle between the interplanetary magnetic field (IMF) and the bow shock normal vector is less than 45°, is particularly turbulent even during steady solar wind conditions. Furthermore, it is permeated both by waves that have been transmitted through the bow shock, as well as by fluctuations that have been generated locally (Blanco-Cano et al., 2006; Lucek et al., 2005).

Upstream of the quasi-parallel bow shock, solar wind ions are reflected forming a region called the ion foreshock which is filled by backstreaming ion populations. These ions can generate various wave modes and—more often than not—ULF waves (Blanco-Cano et al., 2020) which is suggested to be transmitted, through the magnetosheath, into the magnetosphere (Clausen et al., 2009). On the other hand, at the quasi-perpendicular bow shock, the initially reflected ions are mostly heated in the direction perpendicular to the magnetic field exhibiting enhanced temperature anisotropy. This anisotropy can generate transverse ion cyclotron (IC) waves with $\beta \ll 1$ and/or compressive, nonpropagating mirror mode waves with $\beta > 1$ (Génot et al., 2009).

Jets in the magnetosheath are transient localized enhancements in dynamic pressure typically caused by increases in plasma velocity, density, or both (Archer et al., 2012; Karlsson et al., 2015; Plaschke et al., 2013). They are found more frequently downstream of the quasi-parallel shock but are still observed in the quasi-perpendicular magnetosheath (Raptis, Aminalragia-Giamini, et al., 2020; Raptis, Karlsson, et al., 2020;

Vuorinen et al., 2019). However, the jets found in the quasi-parallel region are typically faster and more energetic and as a result may have a more significant magnetospheric effect (Plaschke et al., 2018).

During the past decade, several studies have indicated their importance to magnetospheric dynamics. Jets have been associated with triggering localized magnetopause reconnection (Hietala et al., 2018). One step further, Nykyri et al. (2019) showed that this jet-associated reconnection may lead to enhanced tail flux loading possibly acting as a reconnection trigger for the thin tail current sheet, thus generating substorm injections even during northward IMF. Furthermore, jets have been associated with driving various wave species (Archer et al., 2013; Karlsson et al., 2018; Plaschke & Glassmeier, 2011), causing direct plasma penetration in the magnetosphere (Dmitriev & Suvorova, 2015; Karlsson et al., 2012) and exciting surface eigenmodes through collision with the magnetopause (Archer et al., 2019).

Recently, it has been shown that jets can modify the properties of the ambient plasma in the magnetosheath (Plaschke & Hietala, 2018). Specifically, they may stir the plasma, pushing the slower ambient magnetosheath plasma out of their way. This way the jet creates anomalous flows around it, causing the surrounding plasma to perform a vortical motion. This interaction can cause the background magnetosheath plasma to get significantly decelerated and make the background magnetic field more aligned with the jet's velocity (Karimabadi et al., 2014; Plaschke et al., 2017, 2020). This abrupt change in the magnetic field configuration could possibly favor the generation of waves.

Here we report—for the first time to our knowledge—Pi2 pulsations generated locally in the magnetosheath at the wake of a jet, with absence of any high-energy proton beams or any linkage with the ion foreshock. We show that these pulsations are later observed inside the magnetosphere as field line resonances which raises the question of how exactly they propagated through the magnetopause.

In what follows, we present a structure of this paper. In Section 2, a brief introduction to the data sets and methods used for this study is presented. We then (Section 3) present the detailed observations from both spacecraft at the magnetosheath and inside the magnetosphere. In the detailed discussion that follows (Section 4), we present a working hypothesis for the generation of the pulsations. Finally, we present the conclusions (Section 5) based on our interpretation of these multipoint observations.

2. Data and Methods

We use 3-s resolution measurements of the magnetic field vector from the THEMIS A and D fluxgate magnetometers (Auster et al., 2008). We also use 3-s resolution data of ion flux energy spectrum and velocity vector from the Electrostatic Analyzer (McFadden et al., 2008) on board the same THEMIS probes. Complementary 1-min measurements of solar wind speed and interplanetary magnetic field are obtained from the NASA OMNIWeb database as propagated values at the bow shock nose (https://omniweb.gsfc.nasa.gov/). For the estimation of the magnetic coordinates we used the International Radiation Belt Environment Modeling (IRBEM) library (Bourdarie & O'Brien, 2009) and the TS96 (Tsyganenko & Stern, 1996) external magnetic field model.

For the spectral analysis of the magnetic field measurements we make use of the Continuous Wavelet Transform (CWT—see also Torrence & Compo, 1998) using as mother wavelet the Morlet wavelet (Morlet, 1983) similar to Katsavrias et al. (2015, 2019). Along with the wavelet power spectrum, the global wavelet spectrum is also used which corresponds to the average of the wavelet power spectral density in a specific frequency (f):

$$\overline{W(f)} = \frac{1}{N} \sum_{n=1}^{N} \left\| W_n(f) \right\| \tag{1}$$

where n stands for a localized time index and N corresponds to the length of the time-series. The global wavelet spectrum generally exhibits similar features (and shape) as the corresponding Fourier spectrum.

Furthermore, we make use of the Cross-Wavelet Transform (XWT) and the Wavelet Coherence (WTC) following Katsavrias et al. (2016). The Cross Wavelet Transform (henceforward XWT—see also Grinsted et al. (2004) between two time-series X and Y and their corresponding CWTs is defined as:

$$W_n^{XY}(f) = W_n^X(f) \cdot W_n^Y(f)^* \tag{2}$$

while the phase relationship between the two variables is then defined as:

$$\Phi = tan^{-1}\left[\frac{im(|W_n^{XY}(f)|)}{re(|W_n^{XY}(f)|)}\right] \tag{3}$$

As shown, the XWT examines the causal relationship in the time-frequency space between two time-series searching for regions of high common power and consistent phase relationship.

Finally, the wavelet coherence (hence forward WTC) is an estimator of the confidence level for each detection of a time-space region of consistent phase relationship even if the common power is low. The measure of wavelet coherence closely resembles a localized correlation coefficient in time-frequency space and varies between 0 and 1, corresponding to noncoherent and highly coherent phase relationship, respectively. The statistical significance level of the WTC is estimated using Monte Carlo methods.

3. Detailed Event Analysis

On February 13, 2013 near noon, THEMIS-A (THA) was located in the dayside magnetosheath close to the bow shock (R≈12 R_E and MLT≈10.5), while THEMIS-D (THD) was located inside the dayside magnetosphere near the geostationary orbit (L≈7 and MLT≈12), both following an inbound orbit.

Figure 1 shows (a) 1-min High Resolution OMNI (HRO) magnetic field measurements in GSE/GSM coordinates, (b) the IMF cone angle (θ_{cone}), (c) the estimated upstream wave frequency and (d–f) the magnetopause, bow shock, magnetic field direction and satellite (THA and THD) positions for 11:16, 11:32, and 11:39 respectively. Note that the arrows indicate the x-y direction of the magnetic field, while the z-direction is color coded. The missing data from 11:28 to 11:31 have been interpolated to provide a full characterization of the close to the bow shock conditions. For the modeling of the magnetopause and the bow shock the model of Chao et al. (2002) has been used. Special indication is made for the quasi-parallel (Qpar) bow shock (blue: $\theta_{Bn} < 45°$), while the quasi-perpendicular (Qperp) was separated in two different regions (red: $\theta_{Bn} > 55$ and magenta: $45° < \theta_{Bn} < 55°$), where θ_{Bn} is the angle between the interplanetary magnetic field (IMF) direction and bow shock normal vector. This was done to show the transition region between the Qpar and Qperp configuration which can still have significant foreshock properties (Wilson, 2016) and corresponds to the area where a field-aligned beam (FAB) is commonly observed. Note that the solar wind speed (not shown here) remained constant at ≈360 km/s during the whole time-period shown in Figure 1.

Moreover, the estimation of the upstream wave frequency follows the empirical model by Takahashi et al. (1984):

$$f_{UW}[mHz] = 7.6 \cdot B_0[nT] \cdot cos^2(\theta_{cone}) \tag{4}$$

where B_0 is the IMF strength and θ_{cone} is the IMF cone angle calculated from the 1-min HRO data. As shown, at all three positions, the upstream wave frequency does not exceed 4 mHz.

During 11:37–11:39 UT, THEMIS-A, which was located in the dayside magnetosheath close to the bow shock, we observed a moderate magnetosheath jet with a density increase from approximately 40 to more than 80 particles per cc, maximum pressure at 2 nPa (Figure 2a) and maximum speed of −213 km/s at approximately 11:38 UT (Figure 2b). Note that the average ambient Vx was approximately −78 km/s which means that the jet exhibited an enhancement in Vx by a factor of 2.7, while the average ambient Vy was approximately −41 km/s. Right after the jet, the Vx component of speed dropped to a zero average, with occasionally sunward direction, until approximately 11:46 UT, when another jet occurred. Henceforward we will refer to the 11:39–11:46 UT time-period, which corresponds to the wake of the jet as After-Flow (AF). With the beginning of the AF, all three components of the magnetic field (Figure 2c) exhibited strong disturbances which faded with the beginning of the second jet at approximately 11:46 UT. Panel 2d shows a characteristic high energy ion population which indicates the presence of a significant ion foreshock and therefore shows that THA resides downstream of the quasi-parallel bow shock. This is in agreement with the IMF rotation and the changes in foreshock configuration shown in Figure 1e. A more detailed configuration of the magnetic field direction compared with the flow direction inside the magnetosheath
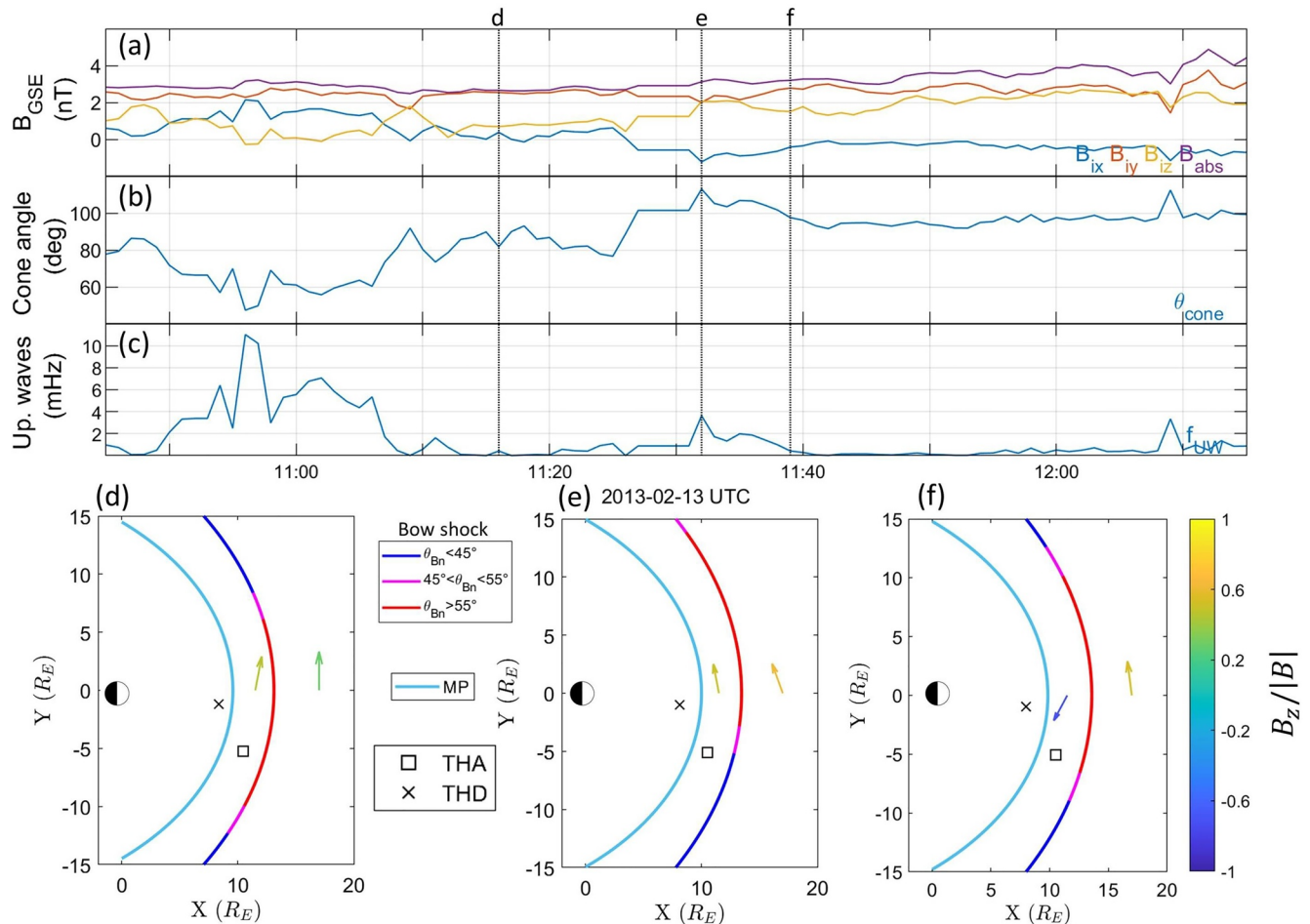
Figure 1. OMINWeb propagated values at the bow shock nose during February 13, 2013. Top to bottom: (a) interplanetary magnetic field vector in GSE coordinates, (b) solar wind cone angle and (c) the estimated upstream wave frequency inferred from the empirical model by Takahashi et al. (1984). The vertical dotted lines correspond to three different timestamps shown in panels (d–f). (d) is at 11:16, (e) at 11:32 and (f) at 11:39. Each of these panels show approximate boundary positions (magnetopause, bow shock) along with different configuration of the bow shock (quasi-parallel, quasi-perpendicular). The arrows, in panels (d–f), indicate the magnetic field direction, both upstream of the bowshock and in the magnetosheath, in the x-y plane, while the normalized Bz component is color-coded. The positions of THA (black square) and THD (black x) are also indicated.

is included in Figure S7 in the Supporting Information. Note that we do not discuss any results close to or after 11:50 UT since THEMIS-A has a short transition from the magnetosheath to the upstream solar wind.

Panel 2e shows the wavelet spectrum of the total magnetic field magnitude measured by THA, accompanied by the global spectrum (left panel) while the red dashed line corresponds to the 95% confidence level. The frequency range of the spectrum covers the 0.5–30 mHz range which corresponds to the Pc4–Pc6 frequency range. In detail, the spectrum exhibits a prominent peak at 2.1 mHz (as indicated by the global spectrum) which spans the whole duration of the quasi-parallel configuration of the magnetosheath with power at $\approx 1000 nT^2$ / Hz. Note that the prominent frequency band in the Pc5 range which occurs during the 11:40–12:00 UT time-period is not discussed as it coincides with the bow shock crossing and, therefore, its validity is dubious. Furthermore, the wavelet spectrum exhibits prominent pulsations in two frequency bands (7.6–9.2 and 12–17 mHz as indicated by the global spectrum). These frequency bands coincide with the AF duration and exhibit global power that exceeds the 100 nT^2 / Hz value. Note that, even though, low-amplitude disturbances occur throughout the whole Qpar configuration, they are considerably below the 95% confidence level. This behavior is consistent even if we filter the time-series in the 7–30 mHz frequency range (see also Figure S1 in the Supporting Information) where the amplitude of the oscillations is approximately two times greater during the AF. The white dashed line in panel 2e corresponds to the
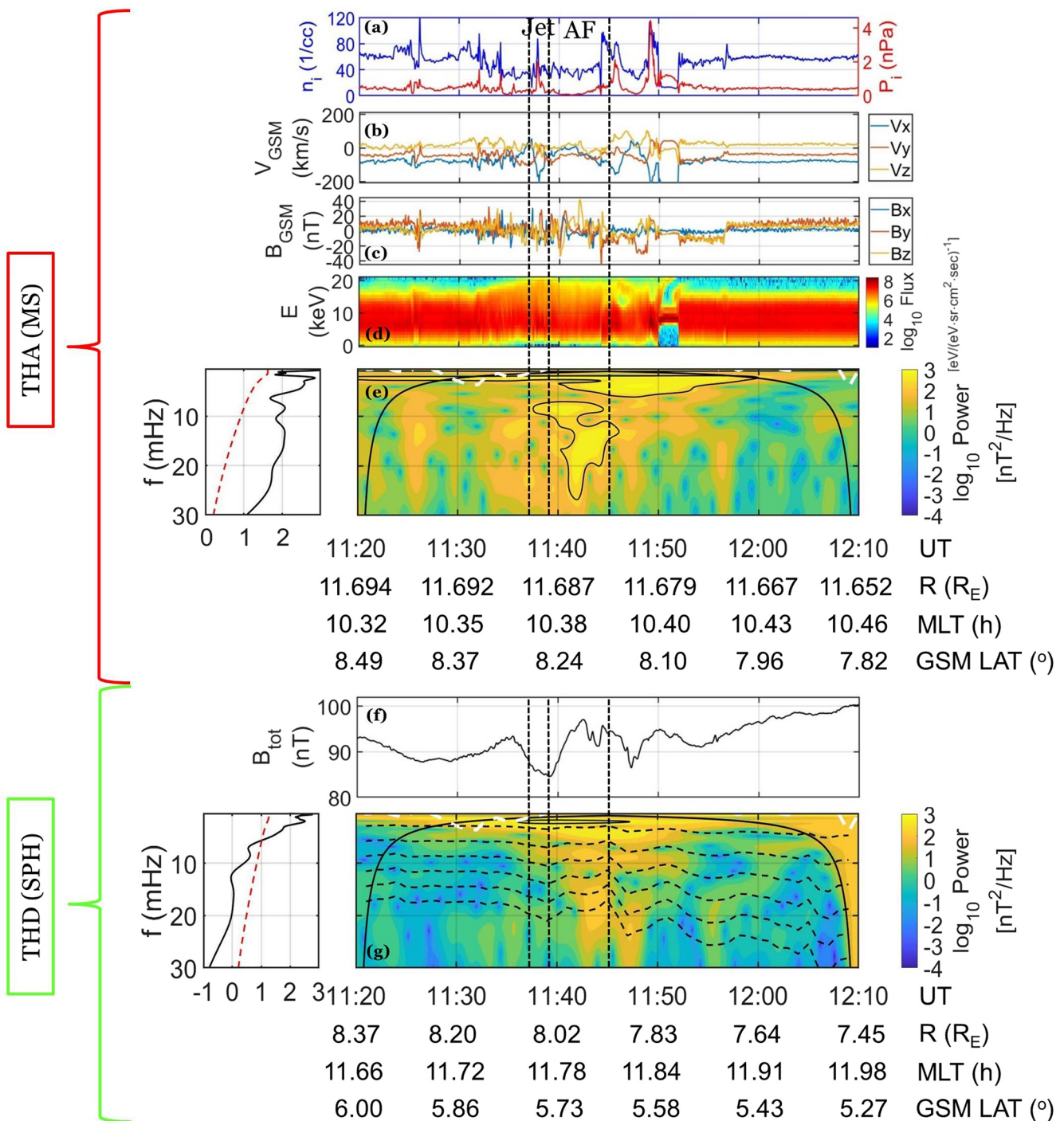
Figure 2. THEMIS A and D observations in the magnetosheath and in the magnetosphere, respectively. Top to bottom: (a) Ion density (blue) and dynamic pressure (red), (b) THA velocity vector in GSM coordinates, (c) THA magnetic field vector in GSM coordinates, (d) THA energy spectrum, (e) wavelet spectrum of the total magnetic field magnitude measured by THA, (f) total magnetic field magnitude measured by THD inside the magnetosphere, and (g) wavelet spectrum of the THD total magnetic field magnitude. Each wavelet spectrum is accompanied by the global spectrum and its 95% confidence level (black solid and dashed red lines in the left panels, respectively). Note that, in both spectra, the frequency axis is inverted with lower frequencies shown at the top of the axis. The black solid line and the black contours in the wavelet spectra correspond to the cone of influence and the 95% confidence level, respectively. The vertical dashed lines correspond to the duration of the jet and its After-Flow (AF). The white dashed lines in the wavelet spectra correspond to the expected frequency of upstream waves while the black dashed lines in the THD spectra correspond to the estimates of the fundamental and the five first harmonics of the field line resonances at the spacecrafts' location.

expected frequency of upstream ULF waves generated in the ion foreshock. As shown, none of the exhibited Pi2 pulsations can be explained by the estimated upstream wave frequency. Furthermore, the ratio of the total electric field over the total magnetic field in the magnetosheath compared to the local Alfvén speed (see Figure S2 in the Supporting Information) indicates that the observed pulsations are fast mode waves.

Panels 2f and g show the time-series and the wavelet spectrum of the total magnetic field magnitude measured by THD, accompanied by the global spectrum (left panel) while the red dashed line corresponds to the 95% confidence level. As shown, there are clear oscillations that coincide with the jet and the AF occurrence. In detail, the wavelet spectrum of THD—which shows many similarities with the one of THA—exhibits a prominent peak at 2 mHz, roughly at the 11:30–11:55 UT period, which coincides with the one at 2.1 mHz exhibited in the magnetosheath. Furthermore, the wavelet spectrum exhibits prominent pulsations in two frequency bands (7–9.7 and 14–20 mHz as indicated by the global spectrum). These frequency bands are in very good agreement with the ones exhibited in the magnetosheath during the AF. They show the same duration and lag at $\approx$2.5 min. Note that even though these frequency bands appear below the 95% confidence level they are not insignificant. If we filter the time-series, we practically exclude the effect of the lower frequencies (which usually appear with higher power) indicating that they are statistically significant (see Figure S1 in the Supporting Information).

Following Archer et al. (2013), we have estimated the field line resonance (FLRs) frequencies using the time of flight approximation:

$$f_{FLR} = \left[2 \cdot \int \frac{ds}{V_A} \right]^{-1} \tag{5}$$

where f_{FLR} is the fundamental FLR frequency, V_A is the Alfvén speed, and the integration is carried out over the entire length of the field line which is estimated using the TS96 model. For the electron density estimation we used a power law distribution:

$$\rho(L,r) = \rho_0(L) \left[\frac{L}{r} \right]^m \tag{6}$$

where r is the geocentric radial distance, L is the equatorial distance to the field line, ρ_0 is the equatorial mass density inferred from THD (since it is very close to the equatorial plane), and the exponent m is taken to be 2 (Denton, 2002). The dashed black lines in Figure 2g indicate the fundamental and the first five harmonics of the FLR at the spacecraft location. As shown, the two prominent frequency bands correspond to the second and fifth harmonics. Note that using various external magnetic field models changed the results by approximately 0.5 mHz at all L-shells (see also Figure S3 in the Supporting Information). Similarly, changing the exponent of the density distribution had negligible effect on the results. Thus, we can assume that the estimated FLRs are broadly correct, even though we do not require precise calculations in this study.

In a more detailed examination, the aforementioned wave activity occurred primarily in the field-aligned component of the magnetic field, peaking in the two frequency bands mentioned above (see also Figure S4 in the Supporting Information). These compressional oscillations suggest that the these Pi2 pulsations are fast Alfvén waves which propagated across the magnetic field. Nevertheless, a mode conversion from fast to shear Alfvén waves should be expected at the location of the THD spacecraft, forming localized features such as FLRs, or differently standing Alfvén waves. These standing waves accompanied by a $90°$ phase relationship between the electric and magnetic field (not shown) are present in the spectrum of the toroidal component at the second harmonic of the FLR in the 9.5–11.5 mHz frequency range.

4. Discussion

As shown in the previous section, on February 13, 2013, THEMIS-A observed a magnetosheath jet at 11:38 UT which was followed by a period of slowed (occasionally sunward directed) ambient plasma which we characterized as After-Flow (AF). The properties of the AF plasma region are very close to the properties one expects from an ambient plasma interacting with a high-speed velocity jet, with de-acceleration of the background plasma and anomalous (possibly even sunward) flow (Plaschke & Hietala, 2018; Plaschke
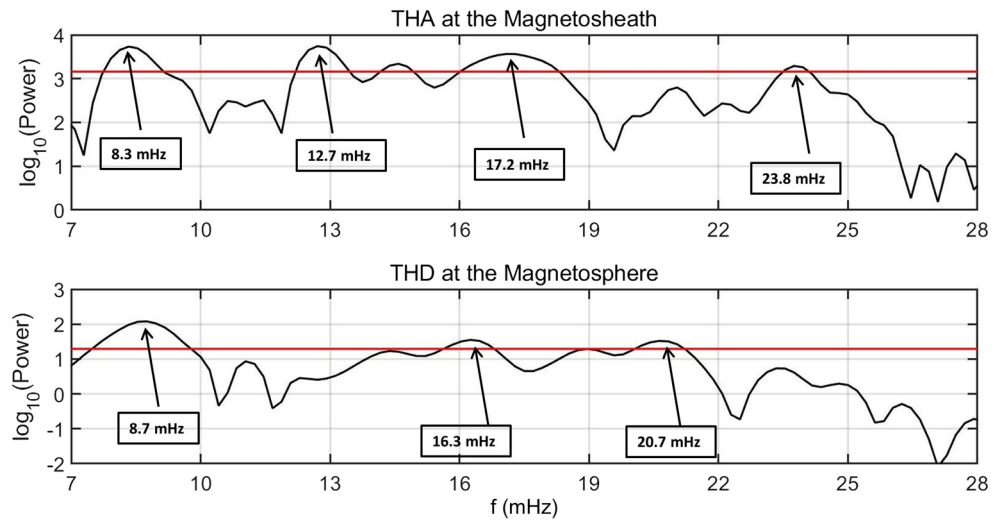
Figure 3. Lomb-Scargle periodogram during the 11:35–11:55 UT time-period for the total magnetic field magnitude measured by THEMIS-A at the magnetosheath (top panel) and THEMIS-D in the magnetosphere (bottom panel). The horizontal red lines correspond to the 95% confidence level. The black boxes highlight the frequency local maxima.

et al., 2020). Moreover, and in agreement with expectations, jets generally do modify the magnetic field on their passage. Indeed, during this period, THEMIS-A magnetometer showed abrupt disturbances which, in the wavelet spectrum, appeared as prominent and irregular pulsations in the Pi2 frequency range and in two frequency bands (7.6–9.2 and 12–17 mHz). Note that Pi2 pulsations are a well-known example of waves triggered by dB/dt, and/or sudden changes in the magnetic field configuration (Keiling & Takahashi, 2011). Especially in the Earth's magnetosphere, they have been associated with other fast plasma flows appearing in the plasma sheet, the Bursty Bulk Flows (BBFs) (Angelopoulos et al., 1992; Kepko et al., 2001; Wang et al., 2015). Of course, there can be no straightforward comparison between the highly turbulent magnetosheath plasma and the plasma sheet, nevertheless, there are some similarities in terms of a fast plasma flow abruptly modifying the magnetic field, which in turn gives birth to Pi2 pulsations.

Another possible origin of these pulsations could be the magnetosheath downstream of the quasi-parallel shock (Schwartz et al., 1996). Nevertheless, both the unfiltered and the filtered magnetic field spectra exhibited these pulsations with significant power (above the 95% confidence level) during the AF duration, only. On the contrary, continuous pulsations in the Pc5 frequency range, which were also observed, roughly covered the whole quasi-parallel magnetosheath. Furthermore, it may be possible that the jet made the magnetic field in the sheath more aligned with its propagation direction and opened connectivity to the ion foreshock from where these pulsations came from (Clausen et al., 2009; Wilson, 2016). Nevertheless, the estimated upstream wave frequencies were considerably below the frequency range under examination and, moreover, the foreshock-sheath connectivity should have produced high energy proton beams which, in this case, are completely absent from THEMIS measurements (see also Figure S5 in the Supporting Information). Finally, even though we have no in situ measurements from the foreshock region that can definitely disprove the foreshock generated pulsations, the aforementioned evidence renders this an unlike scenario.

From all the above, and considering the Pi2 pulsations are isolated to the AF region only, we can conclude that there is a clear link between the local magnetic field disturbance generated by the jet's interaction with the ambient plasma and the observed pulsations, even though we have no indications about the exact physical mechanism that generates them.

Furthermore, these Pi2 frequency bands were later detected in the magnetosphere by THEMIS-D. Thus, in what follows we will focus our discussion on the Pi2 frequency range during the AF.

Figure 3 shows the Lomb-Scargle periodogram in the 7–28 mHz frequency range during the 11:35–11:55 UT time-period for the total magnetic field magnitude measured by THA at the magnetosheath (top panel)
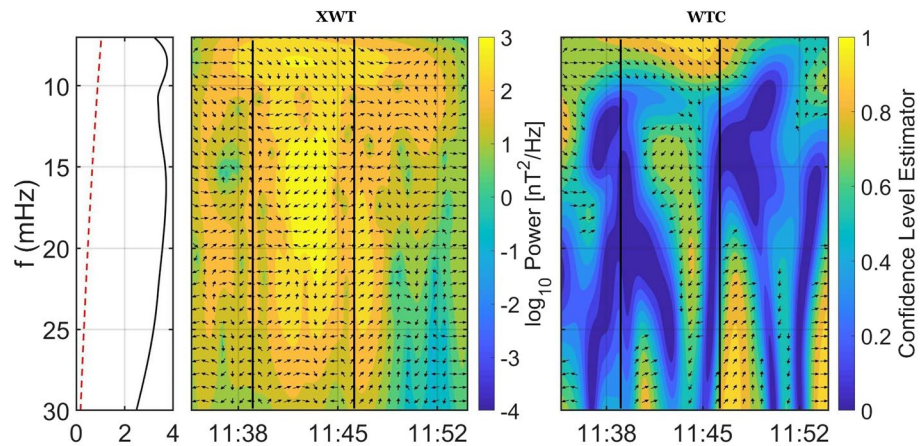
Figure 4. Cross-wavelet (middle panel) and phase coherence (right panel) between the pulsations in the magnetosheath and in the magnetosphere in the 7–30 mHz frequency range. The left panel corresponds to the global spectrum. Note that the frequency axis is inverted with lower frequencies shown at the top of the axis. The color-bar of the Wavelet Coherence corresponds to the confidence level of the phase, obtained by the Monte-Carlo test, and the arrows appearing correspond to a confidence level greater than 0.6. The arrows point to the phase relationship of the two data series in time-frequency space: (a) arrows pointing to the right indicate in-phase behavior; (b) arrows pointing to the left indicate antiphase behavior; (c) arrows pointing downward indicate that the first data set is leading the second by 90°. The vertical black lines mark the duration of the jet's After-Flow (AF).

and THD in the magnetosphere (bottom panel) accompanied by their 95% confidence level. The use of the Lomb/Scargle periodogram (Scargle, 1982), is complementary to the wavelet spectrum as the discrete periodicities in the former sometimes correspond to a range of periodicities in the latter. As shown, the two periodograms exhibit a remarkable similarity and, furthermore, are in good agreement with the corresponding wavelet spectra. In detail, the two periodograms exhibit local peaks that exceed the 95% confidence level at two frequency bands. The first band corresponds to 7.8–9.1 mHz (peak at 8.3 mHz) and 7.6–9.7 mHz (peak at 8.7 mHz) at the magnetosheath and magnetosphere, respectively. The second band corresponds to 16.1–18.2 mHz (peak at 17.2 mHz) and 15.8–16.7 mHz (peak at 16.3 mHz) at the magnetosheath and magnetosphere, respectively.

Figure 4 shows the cross-wavelet and phase coherence between the pulsations in the magnetosheath and in the magnetosphere in the 7–30 mHz frequency range. Similar to the Lomb-Scargle periodograms, the XWT (middle panel of Figure 4) exhibits common power in two frequency bands with peak frequency at 8.5 and 16.3 mHz which is limited inside the AF duration and, moreover, exhibits a statistically significant phase coherence (right panel of Figure 4). In detail, the phase between the two signals is ≈60 and 120° (which corresponds to an estimate of 140 s) for the 8.5 and 16.3 mHz, respectively. Note that this propagation time is in good agreement with the estimated propagation time of a disturbance traveling with Alfvénic speed (see also Figure S6 in the Supporting Information) from the corresponding positions of THA, THD, and THE.

All the above indicate that the Pi2 pulsations detected in the magnetosphere are directly associated with those observed in the magnetosheath. Nevertheless, a question arises from these results concerning the way these pulsations are propagated through the magnetopause. Archer et al. (2019) showed that impulses on the boundary can generate standing waves or eigenmodes of the magnetopause surface, which can later on propagate to the inner magnetosphere. Nevertheless, we have indicated that the Pi2 pulsations observed in this study are locally generated in the magnetosheath by the interaction of the jet with the ambient plasma, since they are not found within the jet itself. Moreover, Archer et al. (2013) showed that the magnetopause acts like a low-pass filter, favoring the excitation of Pc5 and Pc6 pulsations in the compressional components of the magnetic field, while in this study we refer to Pi2 frequencies. Finally, even though a direct penetration of these pulsations through the magnetopause is a possible explanation, this scenario requires much further investigation which is out of scope of this study.

5. Conclusions

On February 13, 2013 near noon, THEMIS-A, which was located in the dayside magnetosheath, observed a magnetosheath jet downstream of the quasi-parallel bow shock. Right after the jet, the After-Flow (AF) was associated with Pi2 pulsations in two frequency bands (7.6–9.2 and 12–17 mHz). It is the first time—to our knowledge—such a wave activity is detected in the magnetosheath. Our results indicate that these pulsations were locally generated, possibly due to the sudden changes in the magnetic field driven by the jet's interaction with the ambient magnetosheath plasma. Furthermore, these pulsations were also detected inside the magnetosphere with a 140-s time-lag, which raises the question of how exactly these pulsations are propagated through the magnetopause.

Data Availability Statement

The authors acknowledge the THEMIS/FGM and THEMIS/ESA teams for the use of the corresponding data sets which can be found online in http://themis.ssl.berkeley.edu/data_products/index.php, the developers of the International Radiation Belt Environment Modeling (IRBEM) library and the NASA/GSFC's Space Physics Data Facility's OMNIWeb service in https://spdf.gsfc.nasa.gov/pub/data/omni/high_res_omni/.

References

Angelopoulos, V., Baumjohann, W., Kennel, C. F., Coroniti, F. V., Kivelson, M. G., Pellat, R., et al. (1992). Bursty bulk flows in the inner central plasma sheet. *Journal of Geophysical Research*, *97*(A4), 4027. https://doi.org/10.1029/91ja02701

Archer, M. O., Hietala, H., Hartinger, M. D., Plaschke, F., & Angelopoulos, V. (2019). Direct observations of a surface eigenmode of the dayside magnetopause. *Nature Communications*, *10*(1). https://doi.org/10.1038/s41467-018-08134-5

Archer, M. O., Horbury, T. S., & Eastwood, J. P. (2012). Magnetosheath pressure pulses: Generation downstream of the bow shock from solar wind discontinuities. *Journal of Geophysical Research*, *117*(A5). https://doi.org/10.1029/2011ja017468

Archer, M. O., Horbury, T. S., Eastwood, J. P., Weygand, J. M., & Yeoman, T. K. (2013). Magnetospheric response to magnetosheath pressure pulses: A low-pass filter effect. *Journal of Geophysical Research: Space Physics*, *118*(9), 5454–5466. https://doi.org/10.1002/jgra.50519

Auster, H. U., Glassmeier, K. H., Magnes, W., Aydogar, O., Baumjohann, W., Constantinescu, D., et al. (2008). The THEMIS fluxgate magnetometer. *Space Science Reviews*, *141*(1–4), 235–264. https://doi.org/10.1007/s11214-008-9365-9

Blanco-Cano, X., Omidi, N., & Russell, C. T. (2006). Macrostructure of collisionless bow shocks: 2. ULF waves in the foreshock and magnetosheath. *Journal of Geophysical Research*, *111*(A10). https://doi.org/10.1029/2005ja011421

Blanco-Cano, X., Preisser, L., Kajdič, P., & Rojas-Castillo, D. (2020). Magnetosheath microstructure: Mirror mode waves and jets during southward IP magnetic field. *Journal of Geophysical Research*, *125*(9). https://doi.org/10.1029/2020ja027940

Bourdarie, S., & O'Brien, T. (2009). International radiation belt environment modeling library. *Space Research Today*, *174*, 27–28. https://doi.org/10.1016/j.srt.2009.03.006

Chao, J., Wu, D., Lin, C.-H., Yang, Y.-H., Wang, X., Kessel, M., et al. (2002). Models for the size and shape of the Earths magnetopause and bow shock. In *Space weather study using multipoint techniques, proceedings of the COSPAR colloquium* (pp. 127–135). Elsevier. https://doi.org/10.1016/s0964-2749(02)80212-8

Clausen, L. B. N., Yeoman, T. K., Fear, R. C., Behlke, R., Lucek, E. A., & Engebretson, M. J. (2009). First simultaneous measurements of waves generated at the bow shock in the solar wind, the magnetosphere and on the ground. *Annales Geophysicae*, *27*(1), 357–371. https://doi.org/10.5194/angeo-27-357-2009

Denton, R. E. (2002). Magnetospheric electron density model inferred from polar plasma wave data. *Journal of Geophysical Research*, *107*(A11). https://doi.org/10.1029/2001ja009136

Dmitriev, A., & Suvorova, A. (2015). Large-scale jets in the magnetosheath and plasma penetration across the magnetopause: Themis observations. *Journal of Geophysical Research: Space Physics*, *120*(6), 4423–4437. https://doi.org/10.1002/2014ja020953

Génot, V., Budnik, E., Hellinger, P., Passot, T., Belmont, G., Trávníček, P. M., et al. (2009). Mirror structures above and below the linear instability threshold: Cluster observations, fluid model and hybrid simulations. *Annales Geophysicae*, *27*(2), 601–615. https://doi.org/10.5194/angeo-27-601-2009

Grinsted, A., Moore, J. C., & Jevrejeva, S. (2004). Application of the cross wavelet transform and wavelet coherence to geophysical time series. *Nonlinear Processes in Geophysics*, *11*(5/6), 561–566. https://doi.org/10.5194/npg-11-561-2004

Hietala, H., Phan, T. D., Angelopoulos, V., Oieroset, M., Archer, M. O., Karlsson, T., & Plaschke, F. (2018). In situ observations of a magnetosheath high-speed jet triggering magnetopause reconnection. *Geophysical Research Letters*, *45*(4), 1732–1740. https://doi.org/10.1002/2017gl076525

Karimabadi, H., Roytershteyn, V., Vu, H. X., Omelchenko, Y. A., Scudder, J., Daughton, W., et al. (2014). The link between shocks, turbulence, and magnetic reconnection in collisionless plasmas. *Physics of Plasmas*, *21*(6), 062308. https://doi.org/10.1063/1.4882875

Karlsson, T., Brenning, N., Nilsson, H., Trotignon, J.-G., Vallières, X., & Facsko, G. (2012). Localized density enhancements in the magnetosheath: Three-dimensional morphology and possible importance for impulsive penetration. *Journal of Geophysical Research*, *117*(A3). https://doi.org/10.1029/2011ja017059

Karlsson, T., Kullen, A., Liljeblad, E., Brenning, N., Nilsson, H., Gunell, H., & Hamrin, M. (2015). On the origin of magnetosheath plasmoids and their relation to magnetosheath jets. *Journal of Geophysical Research: Space Physics*, *120*(9), 7390–7403. https://doi.org/10.1002/2015ja021487

Karlsson, T., Plaschke, F., Hietala, H., Archer, M., Blanco-Cano, X., Kajdič, P., et al. (2018). Investigating the anatomy of magnetosheath jets—MMS observations. *Annales Geophysicae*, *36*(2), 655–677. https://doi.org/10.5194/angeo-36-655-2018

Katsavrias, C., Daglis, I. A., Turner, D. L., Sandberg, I., Papadimitriou, C., Georgiou, M., & Balasis, G. (2015). Nonstorm loss of relativistic electrons in the outer radiation belt. *Geophysical Research Letters*, *42*(24), 10521–10530. https://doi.org/10.1002/2015gl066773

Katsavrias, C., Hillaris, A., & Preka-Papadema, P. (2016). A wavelet based approach to solar–terrestrial coupling. *Advances in Space Research*, *57*(10), 2234–2244. https://doi.org/10.1016/j.asr.2016.03.001

Katsavrias, C., Sandberg, I., Li, W., Podladchikova, O., Daglis, I., Papadimitriou, C., et al. (2019). Highly relativistic electron flux enhancement during the weak geomagnetic storm of April–May 2017. *Journal of Geophysical Research: Space Physics*, *124*(6), 4402–4413. https://doi.org/10.1029/2019ja026743

Keiling, A., & Takahashi, K. (2011). Review of pi2 models. *Space Science Reviews*, *161*(1–4), 63–148. https://doi.org/10.1007/s11214-011-9818-4

Kepko, L., Kivelson, M. G., & Yumoto, K. (2001). Flow bursts, braking, and pi2 pulsations. *Journal of Geophysical Research*, *106*(A2), 1903–1915. https://doi.org/10.1029/2000ja000158

Lucek, E., Constantinescu, D., Goldstein, M., Pickett, J., Pinçon, J., Sahraoui, F., et al. (2005). The magnetosheath. *Space Science Reviews*, *118*(1), 95–152. https://doi.org/10.1007/s11214-005-3825-2

McFadden, J. P., Carlson, C. W., Larson, D., Ludlam, M., Abiad, R., Elliott, B., et al. (2008). The THEMIS ESA plasma instrument and in-flight calibration. *Space Science Reviews*, *141*(1–4), 277–302. https://doi.org/10.1007/s11214-008-9440-2

Morlet, J. (1983). Sampling theory and wave propagation. In *Issues in acoustic signal—image processing and recognition* (pp. 233–261). Springer Berlin Heidelberg. https://doi.org/10.1007/978-3-642-82002-1_12

Nykyri, K., Bengtson, M., Angelopoulos, V., Nishimura, Y., & Wing, S. (2019). Can enhanced flux loading by high-speed jets lead to a substorm? Multipoint detection of the christmas day substorm onset at 08:17 UT, 2015. *Journal of Geophysical Research: Space Physics*, *124*(6), 4314–4340. https://doi.org/10.1029/2018ja026357

Plaschke, F., & Glassmeier, K.-H. (2011). Properties of standing kruskal-schwarzschild-modes at the magnetopause. *Annales Geophysicae*, *29*(10), 1793–1807. https://doi.org/10.5194/angeo-29-1793-2011

Plaschke, F., & Hietala, H. (2018). Plasma flow patterns in and around magnetosheath jets. *Annales Geophysicae*, *36*(3), 695–703. https://doi.org/10.5194/angeo-36-695-2018

Plaschke, F., Hietala, H., & Angelopoulos, V. (2013). Anti-sunward high-speed jets in the subsolar magnetosheath. *Annales Geophysicae*, *31*(10), 1877–1889. https://doi.org/10.5194/angeo-31-1877-2013

Plaschke, F., Hietala, H., Archer, M., Blanco-Cano, X., Kajdič, P., Karlsson, T., et al. (2018). Jets downstream of collisionless shocks. *Space Science Reviews*, *214*(5), 1–77. https://doi.org/10.1007/s11214-018-0516-3

Plaschke, F., Jernej, M., Hietala, H., & Vuorinen, L. (2020). On the alignment of velocity and magnetic fields within magnetosheath jets. *Annales Geophysicae*, *38*, 287–296. https://doi.org/10.5194/angeo-38-287-2020

Plaschke, F., Karlsson, T., Hietala, H., Archer, M., Vörös, Z., Nakamura, R., et al. (2017). Magnetosheath high-speed jets: Internal structure and interaction with ambient plasma. *Journal of Geophysical Research: Space Physics*, *122*(10), 10–157. https://doi.org/10.1002/2017ja024471

Raptis, S., Aminalragia-Giamini, S., Karlsson, T., & Lindberg, M. (2020). Classification of magnetosheath jets using neural networks and high resolution omni (HRO) data. *Frontiers in Astronomy and Space Sciences*, *7*, 24. https://doi.org/10.3389/fspas.2020.00024

Raptis, S., Karlsson, T., Plaschke, F., Kullen, A., & Lindqvist, P.-A. (2020). Classifying magnetosheath jets using mms: Statistical properties. *Journal of Geophysical Research: Space Physics*, *125*(11), e2019JA027754. https://doi.org/10.1029/2019ja027754

Scargle, J. D. (1982). Studies in astronomical time series analysis. II—Statistical aspects of spectral analysis of unevenly spaced data. *The Astrophysical Journal*, *263*, 835. https://doi.org/10.1086/160554

Schwartz, S. J., Burgess, D., & Moses, J. J. (1996). Low-frequency waves in the Earth's magnetosheath: Present status. *Annales Geophysicae*, *14*(11), 1134–1150. https://doi.org/10.1007/s00585-996-1134-z

Takahashi, K., McPherron, R. L., & Terasawa, T. (1984). Dependence of the spectrum of pc 3–4 pulsations on the interplanetary magnetic field. *Journal of Geophysical Research*, *89*(A5), 2770. https://doi.org/10.1029/ja089ia05p02770

Torrence, C., & Compo, G. P. (1998). A practical guide to wavelet analysis. *Bulletin of the American Meteorological Society*, *79*(1), 61–78. https://doi.org/10.1175/1520-0477(1998)079<0061:apgtwa>2.0.co;2

Tsyganenko, N., & Stern, D. (1996). Modeling the global magnetic field of the large-scale birkeland current systems. *Journal of Geophysical Research*, *101*, 27187–27198. https://doi.org/10.1029/96JA02735

Vuorinen, L., Hietala, H., & Plaschke, F. (2019). Jets in the magnetosheath: Imf control of where they occur. *Annales Geophysicae*, *37*, 689–697. https://doi.org/10.5194/angeo-37-689-2019

Wang, G. Q., Ge, Y. S., Zhang, T. L., Nakamura, R., Volwerk, M., Baumjohann, W., et al. (2015). A statistical analysis of pi2-band waves in the plasma sheet and their relation to magnetospheric drivers. *Journal of Geophysical Research: Space Physics*, *120*(8), 6167–6175. https://doi.org/10.1002/2014ja020753

Wilson, L. B. (2016). Low frequency waves at and upstream of collisionless shocks. In *Low-frequency waves in space plasmas* (pp. 269–291). John Wiley & Sons, Inc. https://doi.org/10.1002/9781119055006.ch16